First frequency-domain phenomenological model of the multipole asymmetry in gravitational-wave signals from binary-black-hole coalescence

Shrobana Ghosh,[1,2,3] Panagiota Kolitsidou,[1,4] and Mark Hannam[1]

[1]*School of Physics and Astronomy, Cardiff University, Cardiff CF24 3AA, United Kingdom*
[2]*Max Planck Institute for Gravitational Physics (Albert Einstein Institute), Callinstrasse 38, D-30167 Hannover, Germany*
[3]*Leibniz Universitaat Hannover, 30167 Hannover, Germany*
[4]*School of Physics and Astronomy and Institute for Gravitational Wave Astronomy, University of Birmingham, Edgbaston, Birmingham B15 2TT, United Kingdom*

(Received 6 November 2023; accepted 19 December 2023; published 30 January 2024)

Gravitational-wave signals from binaries that contain spinning black holes in general include an asymmetry between the $+m$ and $-m$ multipoles that is not included in most signal models used in LIGO-Virgo-KAGRA analysis to date. This asymmetry manifests itself in out-of-plane recoil of the final black hole and its inclusion in signal models is necessary both to measure this recoil, but also to accurately measure the full spin information of each black hole. We present the first model of the antisymmetric contribution to the dominant coprecessing-frame signal multipole throughout inspiral, merger, and ringdown. We model the antisymmetric contribution in the frequency domain, and take advantage of the approximations that the antisymmetric amplitude can be modeled as a ratio of the (already modeled) symmetric amplitude, and analytic relationships between the symmetric and antisymmetric phases during the inspiral and ringdown. The model is tuned to single-spin numerical-relativity simulations up to mass-ratio 8 and spin magnitudes of 0.8, and has been implemented in a recent phenomenological model for use in the fourth LIGO-Virgo-KAGRA observing run. However, the procedure described here can be easily applied to other time- or frequency-domain models.

DOI: 10.1103/PhysRevD.109.024061

I. INTRODUCTION

The LIGO-Virgo-KAGRA collaboration has published ~90 gravitational-wave (GW) observations [1–3] since the first detection in 2015 [4]. The majority of these have been from binary black holes (BBHs), from which we are beginning to infer the astrophysical distribution of black-hole masses and spins [5–8] and references therein. So far population inference has had to rely on limited spin information from each binary; to measure the magnitude and orientation of both spins we typically require louder signals than in most of those observed so far [9,10]. We also require sufficiently accurate and physically complete theoretical waveform models. One physical effect that is necessary to measure the full spin information is an asymmetry in the signals' multipolar structure that is not included in the standard full inspiral-merger-ringdown models of `PHENOM` [11–22] or `SEOBNR` [23–29] family used in current LIGO-Virgo-KAGRA analyses.

A non-eccentric BBH is characterized by the black-hole masses m_1 and m_2, and each black hole's angular momentum, $\mathbf{S}_i$, which are usually represented in geometric units as the dimensionless vectors $\boldsymbol{\chi}_i = \mathbf{S}_i/m_i^2$. The dominant effect of the spins on the GW signal is due to the spin components aligned with the binary's orbital angular momentum, which affect the rate of inspiral, and can therefore be measured through their effect on the signal's phase. The remaining (in-plane) spin components have little effect on the inspiral rate. They instead induce orbital and spin precession, which lead to modulations in the signal's amplitude and phase [30]. In most cases this is a weaker contribution to the signal and more difficult to measure, in turn making it difficult to measure the full spin information of the binary. Spin misalignment also leads to an asymmetry in the power emitted above and below the orbital plane, and can lead to large out-of-plane recoils of the final black hole [31]. Most signals to date have been too weak to observe precession and recoil (with the notable exception of several analyses of the signal GW200129_065458 signal—which we refer to

as GW200129 in the rest of the text) [3,32,33], but more signals with measurable spin misalignment are expected as detector sensitivities improve.

Most current generic-binary models separately consist of a model of the signal in a non-inertial frame that tracks the precession of the orbital plane (a "coprecessing" frame), and a model of the time- or frequency-dependent precession angles. If the signal is decomposed into spin-weighted spherical harmonics, then the dominant contributions in the coprecessing frame are the $(\ell = 2, |m| = 2)$ multipoles. As discussed in more detail in Sec. II, current Phenom and effective-one-body (EOB) models assume the symmetry $h^{\rm CP}_{22} = h^{\rm CP*}_{2,-2}$ in the coprecessing frame. Precessing binaries also include an antisymmetric contribution. There have been indications for some time that neglecting this contribution could lead to measurement biases [34,35], and more recently explicit examples of such biases have been found [36]. One model that does include the antisymmetric contribution is the NR surrogate model NRSur7dq4 [37], and this likely plays an important role in being able to accurately infer the primary spin in GW200129 [32,33], demonstrating the need to include the antisymmetric contribution in Phenom and EOB models.

In this paper we present a simple method to model the antisymmetric contribution to the $(\ell = 2, |m| = 2)$ coprecessing-frame multipoles, taking into account the phenomenology of how the antisymmetric contribution depends on the in-plane spin direction and relates to the symmetric contribution. Note that all of the examples shown in this paper are constructed using either numerical relativity waveforms or post-Newtonian estimates and that the model introduced here is versatile in that it can be integrated into any frequency-domain approximant.

To motivate our focus on only the antisymmetric contribution to the dominant multipoles, Fig. 1 shows the frequency-domain amplitude of the coprecessing-frame multipoles for a signal with mass-ratio $q = m_1/m_2 = 2$, spin on the larger black hole of $\chi = 0.8$, and spin misalignment with the orbital angular momentum of $\theta_{\rm LS} = 90°$, i.e., the spin initially lies entirely in the orbital plane. (This is case `CF_38` in Ref. [38].) We see that the antisymmetric (2, 2) amplitude is of comparable strength to the symmetric (3, 3); since the (3, 3) extends to higher frequencies, it will contribute more power than the antisymmetric (2, 2) at high masses, and comparable power in low-mass systems. The next-strongest antisymmetric contribution is to the (3, 3), and we see that this is significantly weaker than the symmetric (4, 4). This suggests that any model that includes symmetric contributions up to $\ell \leq 4$ need only include the dominant (2, 2) antisymmetric contribution. If we wish to accurately model the signal to the level of the symmetric (5, 5) contribution, then we must also include the antisymmetric (3, 3). Current Phenom models include symmetric multipoles up to $\ell = 4$, and so we limit our attention to only the dominant antisymmetric contribution.

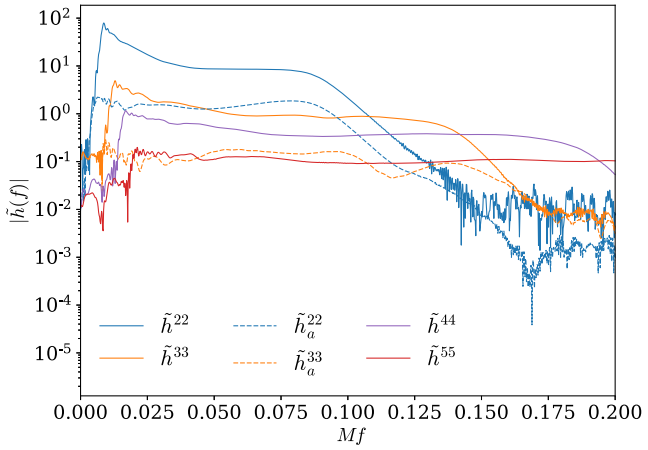

FIG. 1. Frequency-domain amplitude of coprecessing-frame symmetric and antisymmetric contributions for a $(q = 2, \chi = 0.8, \theta_{\rm LS} = 90°)$ configuration. The figure shows the symmetric contributions to (2, 2), (3, 3), (4, 4), and (5, 5), and the antisymmetric contributions to (2, 2) and (3, 3).

[Note that the antisymmetric (3, 3) multipole is also weaker than the symmetric (2, 1) and (3, 2) in this configuration.]

We find that we can model the (2, 2) antisymmetric contribution using numerical relativity (NR) simulations that cover only the reduced parameter space of the binary's mass ratio, the larger black hole's spin magnitude, and its misalignment angle; to a first approximation we do not need to sample the in-plane spin direction, which can be treated analytically. A more complete model that includes subdominant in-plane-spin-direction effects and two-spin effects is left to future work.

In Sec. II we explain the motivation behind our modeling approach. We describe the preparation of the NR data that we used to calibrate our model in Sec. III. In Sec. IV we construct a model of the ratio of the antisymmetric and symmetric amplitudes, and in Sec. V, we present our method to construct the antisymmetric phase from the symmetric phase and the precession angle, α. We discuss the accuracy of our prescription in Sec. VI.

II. ASYMMETRY BACKGROUND

An aligned-spin binary is invariant under reflection across the orbital plane. If we choose a coordinate system where the orbital plane is the x-y plane and perform a decomposition of the gravitational-wave signal into spin-weighted spherical harmonics, then this symmetry arises in the signal multipoles as

$$h_{\ell,m}(t) = (-1)^{\ell} h^*_{\ell,-m}(t). \tag{1}$$

This relationship is useful when constructing a model of the multipoles of an aligned-spin binary: we need only explicitly model the positive-m multipoles, and the negative-m multipoles follow from Eq. (1).

When the spins are not aligned with the orbital angular momentum, both the spins and the orbital plane may precess [30,39]. In systems with misaligned spins Eq. (1) no longer holds, even if there is no orbital precession. The simplest illustration of this is the "superkick" configuration [31,40,41]: here the black holes are of equal mass and of equal spin, and the spins lie in the orbital plane but point in opposite directions. The symmetry of this system implies that the orbital plane does not precess, and although the spins will precess *in the orbital plane*, they both precess at the same rate and so remain oppositely directed to each other, so that the vector sum of the two spins is zero at all times. Although the direction of the orbital plane remains fixed, emission of linear momentum perpendicular to the orbital plane causes the entire system to move up and down. This linear momentum emission and "bobbing" [42] manifests itself in the gravitational-wave signal as an asymmetry in the positive- and negative-m multipoles, i.e., a violation of Eq. (1) [31].

The symmetry of Eq. (1) will remain broken regardless of any rotations performed on the multipoles [43]. This point becomes important when constructing signal models, where we regularly make use of a "coprecessing frame." In this frame the signal during the inspiral can be approximated as that of a nonprecessing binary [44] and so many current waveform models are split into a model for aligned-spin binaries and a model for the precession dynamics, and the precession dynamics are then used to "twist up" a nonprecessing-binary waveform to produce the complete precessing-binary waveform [13,15,16,19,24,25,28,45,46]. However, since the nonprecessing-binary waveform respects the symmetry in Eq. (1), the model cannot reproduce the asymmetry that should be present in the true precessing-binary signal.

Several studies have considered the impact of neglecting these multipole asymmetries. Reference [35] compares the multipoles from precessing-binary waveforms with those from nominally equivalent nonprecessing binaries, to test a number of assumptions that go into the construction of many commonly used waveform models, including neglecting the multipole asymmetry. Reference [34] compares NR waveforms from configurations with different in-plane spin directions and magnitudes, and argues that neglecting the multipole asymmetry may lead to parameter biases even at moderate SNRs, and that including the multipole asymmetry will be necessary to clearly measure in-plane spins and identify precessing systems. Finally, Ref. [36] uses the surrogate model NRSur7dq4 to identify the level of bias in binary measurement examples, and confirms that neglecting the multipole asymmetry leads to biases in measuring in-plane spins (but the masses and effective aligned spin $\chi_{\rm eff}$ are less affected). They also confirm the importance of the multipole asymmetry in precession measurements, showing that it had a significant impact on measurement of the properties of the signal GW200129 [32,33].

In the next section we will summarize the leading-order PN contribution to the asymmetry, which provides some insight into the phenomenology of the multipole asymmetry, and also motivate our modeling procedure. Although the multipole asymmetry has been known for some time, and indeed is included in the standard PN expressions that we use here, and is also discussed in detail in Ref. [43], we are not aware of any prior treatment that discusses the amplitude and phasing of the antisymmetric (2, 2) contribution in relation to the symmetric contribution, or notes the simple dependence of the relative phase between different in-plane spin directions, which is a key feature of the asymmetry that we exploit in constructing our model.

A. Inspiral

To gain insight into the phenomenology of the multipole asymmetry during the inspiral, we consider the leading-order post-Newtonian contributions to a binary where only one black hole is spinning and the spin lies entirely in the orbital plane. The binary consists of two black holes with masses m_1 and m_2 and the dimensionless spin on the primary is $\chi = S_1/m_1^2$, where S_1 is the magnitude of the black hole's angular momentum. We use the post-Newtonian expressions from Ref. [47], where in this single-spin case the symmetric and antisymmetric spin contributions are $\chi_s = \chi_a = \chi/2$. The in-plane spin components incline the total angular momentum $\mathbf{J}$ with respect to the normal to the orbital plane (and direction of the Newtonian orbital angular momentum, $\mathbf{L}$) by an angle ι, and the azimuthal precession angle of $\mathbf{L}$ around $\mathbf{J}$ is α; this is also the azimuthal angle of the total in-plane spin. As such, if we choose the instantaneous orbital plane to coincide with the x-y plane, then the entirely in-plane spin can be written as $\boldsymbol{\chi} = \chi(\cos(\alpha), \sin(\alpha), 0)$.

We start with the multipole h_{22} as given in Eq. (B1) in Ref. [47]. Requiring symmetry due to exchanging black holes [see the discussion prior to Eq. (4.15) in the same paper], leads to the relation $h_{\ell m}(\Phi) = (-1)^{\ell+m} h^*_{\ell -m} \times (\Phi + \pi)$, where Φ is the orbital phase. We can enter the instantaneous orbital plane by setting $\iota = \alpha = 0$, and from our choice of spin we can then substitute $\chi_{ax} = \chi_{sx} = \chi\cos(\alpha)/2$ and $\chi_{ay} = \chi_{sy} = \chi\sin(\alpha)/2$; see Sec. VI B of Ref. [48] for details. We then have an approximation to the symmetric and antisymmetric contributions to the signal in the coprecessing frame, $h_{22}^{\rm CP,s} = (h_{22}^{\rm CP} + h_{2-2}^{*\rm CP})/2$ and $h_{22}^{\rm CP,a} = (h_{22}^{\rm CP} - h_{2-2}^{*\rm CP})/2$, up to $O(v^4)$,

$$h_{22}^{\rm CP,s} = A\left(1 + \frac{(55\eta - 107)v^2}{42}\right) e^{-2i\Phi}, \tag{2}$$

$$h_{22}^{\rm CP,a} = A\frac{(1+\delta)\chi v^2}{4} e^{-i(\Phi+\alpha)}, \tag{3}$$

where the overall amplitude is $A = \sqrt{64\pi/5} M\eta v^2/D_L$, M is the total mass, $\eta = m_1 m_2/M^2$ is the symmetric mass

ratio, $\delta = (m_1 - m_2)/M$, v is the relative speed of the two black holes, and D_L is the luminosity distance to the source. Note that in Ref. [47] the symbol Φ denotes the orbital phase in the instantaneous orbital plane, but here we use it to denote the total orbital phase that enters in the waveform.

We may immediately note several important features from Eqs. (2) and (3). The spin does not enter the amplitude of the symmetric contribution at this order. The antisymmetric contribution enters at $O(v^2)$ lower than the symmetric contribution. We see that we may also consider the antisymmetric amplitude $|h_{22}^{\mathrm{CP,a}}|$ as a simple rescaling of the symmetric amplitude, $|h_{22}^{\mathrm{CP,s}}|$.

The in-plane spin direction, α, does not enter into the amplitude of the antisymmetric contribution, but it does modify the phase. The physical interpretation is that the phase of the antisymmetric contribution depends on the direction of the in-plane spin relative to the separation vector of the two black holes. This will vary with the orbital phase, Φ, but also the (slower) precession rotation of the spin, given by α. This is also consistent with the observation in studies of out-of-plane recoil, that the recoil amplitude depends sinusoidally on the initial direction of the in-plane spin [31].

Finally, we note a key observation for the model that we will produce: if we modify the initial in-plane spin direction by $\Delta\alpha$, this will induce a simple overall phase shift in the antisymmetric contribution, $h_{22}^{\mathrm{CP,a}}$. This suggests that, given a set of single-spin NR waveforms that cover the parameter space of mass ratio, aligned-spin magnitude and in-plane spin magnitude, we will have enough information to build a model of the antisymmetric contribution to single-spin waveforms *without the need to also sample multiple initial in-plane spin directions*. We have just such a set of waveforms to hand, as used to construct the first NR-tuned full inspiral-merger-ringdown model of (the symmetric contribution to) precessing-binary waveforms [48], and discussed in Ref. [38].

B. Merger and ringdown

Before proceeding to construct a model, we consider the phenomenology of the antisymmetric contribution through merger and ringdown, and inspect which inspiral features hold for the entire waveform.

One of the main features of the antisymmetric contribution that we see in the leading-order inspiral single-spin expressions (2) and (3) is that an in-plane rotation of the spin by an angle $\Delta\alpha$ results in a corresponding shift in the antisymmetric (2, 2) phase by $\Delta\alpha$. This is evident from Fig. 2; the two configurations considered here correspond to the superkick configuration described earlier. $\vec{S}_1^{\perp}$ denotes the initial in-plane spin vector of the primary and $\vec{r}_{12}$ is the initial separation vector pointing from the primary to the secondary. It is clear that the asymmetry phase for a configuration with $\vec{S}_1^{\perp} \perp \vec{r}_{12}$ can be easily produced by applying a phase shift of $\pi/2$ to the antisymmetric waveform of a configuration with $\vec{S}_1^{\perp} \parallel \vec{r}_{12}$. We note that the simple phase relationship does not appear to hold as well through merger and ringdown, but the deviation is small enough that this could be due to numerical error, and requires more detailed study in future.

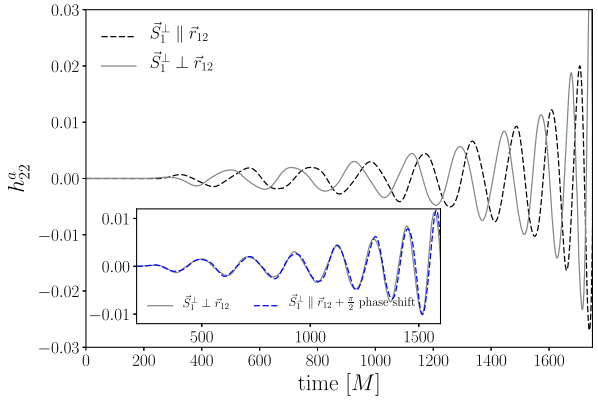

FIG. 2. Antisymmetric waveform constructed from NR waveforms for two superkick configurations in the time domain, $\vec{S}_1^{\perp} \| \vec{r}_{12}$ in dashed black and $\vec{S}_1^{\perp} \perp \vec{r}_{12}$ in solid gray, shows a constant phase offset of $\pi/2$. Inset: dashed blue line shows that the antisymmetric waveform for $\vec{S}_1^{\perp} \perp \vec{r}_{12}$ can be constructed by just applying a $\pi/2$ phase shift to the $\vec{S}_1^{\perp} \| \vec{r}_{12}$ waveform even in the strong-field regime close to merger ($t_{\mathrm{merger}} = 1784M$).

A second key feature of the antisymmetric contribution is that its frequency is roughly half that of the symmetric contribution (plus a small correction from the spin-precession rate $\dot{\alpha}$). Figure 3 shows the time-domain GW frequency of the symmetric and antisymmetric contributions for a configuration where only the larger black hole

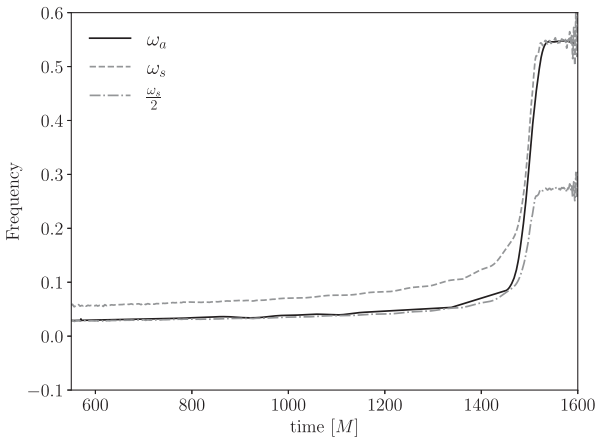

FIG. 3. The symmetric and antisymmetric frequencies obtained from NR data of a $(q = 2, \chi = 0.7, \theta_{\mathrm{LS}} = 90°)$ configuration. During inspiral the antisymmetric frequency, ω_a, is about half of the symmetric frequency, ω_s (or nearly equal to the orbital frequency), and close to merger quickly catches up with the symmetric frequency. As expected from perturbation theory, $\omega_s = \omega_a$ during ringdown.

is spinning, with the spin ($\chi = 0.7$) entirely in plane. We see that during the inspiral the antisymmetric frequency is approximately half that of the symmetric, as we expect.

During ringdown the two frequencies are equal. This is consistent with our expectations from perturbation theory. In the ringdown, where perturbation theory results are applicable, the ($\ell = 2, m = \pm 2$) multipoles will have the same (constant) frequency, and will decay exponentially at the same rate. We therefore expect both the symmetric and antisymmetric combinations of h_{22} and $h_{2,-2}$ to have the same frequency, and for the ratio of the symmetric and antisymmetric amplitudes to be constant throughout the ringdown.

The third property we took from the inspiral expressions (2) and (3) was that the antisymmetric amplitude can be considered as a rescaling of the symmetric amplitude. Figure 4 illustrates that this holds for the entire waveform. It shows the frequency-domain ampiltude of the symmetric and antisymmetric (2, 2) contributions for a configuration with ($q = 1, \chi = 0.4, \theta_{\rm LS} = 60°$), case CF_7 in Ref. [38]. We see in particular that the turnover to ringdown occurs at the same frequency (the ringdown frequency is at $fM \sim 0.09$ for this configuration). We also see that, as discussed above, the symmetric and antisymmetric contributions decay at the same rate.

We will now exploit these features to construct a model for the antisymmetric amplitude and phase.

C. Structure of the model

Based on the observations in the previous section we construct an approximate model of the antisymmetric contribution to the (2, 2) multipole in the coprecessing frame as follows. We start with a model for the symmetric contribution, which provides us with the symmetric amplitude, $A_s(f)$, and symmetric phase, $\phi_s(f)$. In the examples we consider here the symmetric contribution is calculated from NR waveforms. In a full model, we would start with the symmetric contribution from an already existing model. An explicit example is the multimode precessing-binary model described in Ref. [49], but the antisymmetric model described in this paper can be applied to any existing frequency-domain precessing-binary model that separately provides $A_s(f)$, and symmetric phase, $\phi_s(f)$, and the precession angle $\alpha(f)$, as we describe below.

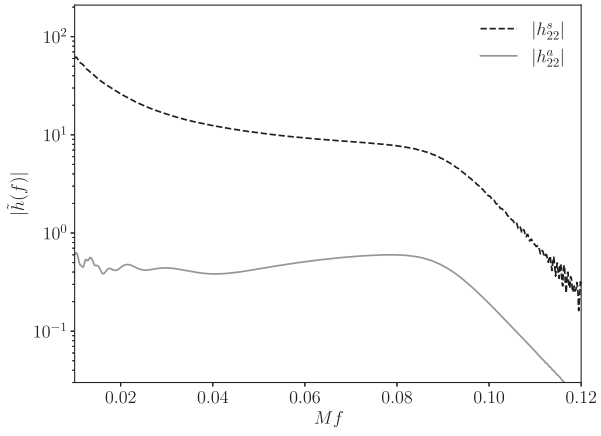

FIG. 4. The amplitude of the ($l = 2, m = 2$) symmetric and the antisymmetric waveform in the frequency-domain coprecessing frame for a ($q = 1, \chi_1 = 0.4, \theta_{LS} = 60°$) NR simulation.

To construct the antisymmetric amplitude, $A_a(f)$, we model the ratio $\kappa(f) = A_a(f)/A_s(f)$. In the inspiral we use a post-Newtonian estimate of the amplitude ratio, and find that we can model the amplitude ratio accurately through to the ringdown by adding only one higher-order term, which we fit to our NR data. In the ringdown we treat the amplitude ratio as a constant, as motivated in the previous section. The amplitude model is presented in Sec. IV.

To construct the antisymmetric phase, during the inspiral we combine the symmetric phase, $\phi_s(f)$, and the precession angle $\alpha(f)$, as prescribed by Eq. (3), i.e., $\phi_a(f) \sim \phi_s(f)/2 + \alpha(f)$. In the merger-ringdown the antisymmetric phase will behave as $\phi_a(f) \sim \phi_s(f)$. We apply an overall time and phase shift to smoothly connect these two functional forms at some transition frequency. We note that we find that it is possible to produce an accurate model of the antisymmetric phase $\phi_a(f)$ using the same transition function for any binary, i.e., the parameters of the transition function do not need to be fit across the binary parameter space. The phase model is presented in Sec. V.

III. NUMERICAL RELATIVITY DATA

The model is tuned to 80 single-spin NR waveforms generated using the BAM code [50,51]. They cover mass ratios $q = \{1, 2, 4, 8\}$, spin magnitudes on the larger black holes of $\chi_1 = \{0.2, 0.4, 0.6, 0.8\}$, and angles of spin misalignment with the orbital angular momentum of $\theta_{\rm LS} = \{30°, 60°, 90°, 120°, 150°\}$. In labeling the configurations, the cases are ordered according to the mass ratios, then the spin magnitudes, then the misalignment angles; for example, case 57 corresponds to ($q = 4, \chi_1 = 0.8$, $\theta_{\rm LS} = 60°$). This is the same indexing as in Ref. [38], which provides full details on the catalog of simulations. To motivate the model and test our modeling assumptions we have also used families of simulations that consider variations in the initial in-plane-spin direction, based on those in Ref. [34]. One notable addition to this set were simulations of superkick configurations where the black holes were given an additional out-of-plane momentum, to remove a secular drift in the center of mass.

Several processing steps are performed to prepare the NR data for modeling, using the tools in Ref. [52]. We start with the waveform data for the $\ell = 2$ multipoles of the Weyl scalar, $\psi_{4,2m}$, in an inertial frame. We apply a Hann window to remove "junk" radiation from the beginning of the waveforms (a nonphysical artifact of the initial data), and to remove numerical noise in the post-ringdown waveform. Furthermore, to ensure that the frequency-domain step size is

sufficiently small, the time-domain data are padded with zeros to the right. More details are given in Ref. [38].

We then transform to a frame that tracks $\hat{J}(t)$; as described in Ref. [48], this retains the approximation that the direction of $\hat{J}(t)$ is constant throughout the waveform. Modeling deviations from this approximation are left to future work and are discussed further in Ref. [48], along with the procedure to track $\hat{J}(t)$ and perform this transformation. At the level of approximation and accuracy of the antisymmetric model presented here, we do not expect this approximation to have any appreciable effect on the final model. We then transform the $\psi_{4,2\pm2}$ multipoles to a coprecessing frame, the "quadrupole-aligned" (QA) [53] or "optimal emission direction" [54,55] frame. In this frame the multipoles are significantly simplified, with the $(l=2,|m|=2)$ multipoles having the strongest amplitude and the precession-induced modulations minimized.

The $(2,\pm2)$ multipoles of time-domain coprecessing frame Ψ_4 are now transformed to the frequency domain,

$$\tilde{\psi}^{\rm CP}_{4,2\pm2}(f) = \int \psi^{\rm CP}_{4,2\pm2}(t) e^{-2\pi i f t} dt. \tag{4}$$

To compute the strain, we note that $\Psi_4(t) = -\ddot{h}(t)$, so in the frequency domain we may write,

$$\tilde{h}^{\rm CP}_{2,\pm2}(f) = -\frac{\tilde{\psi}^{\rm CP}_{4,2\pm2}(f)}{\omega^2}, \tag{5}$$

where $\omega = 2\pi f$. The antisymmetric and symmetric components of the waveform in the QA frame are computed from

$$\tilde{h}^{\rm NR}_s(f) = \frac{1}{2}(\tilde{h}^{\rm CP}_{2,2} + \tilde{h}^{*\rm CP}_{2,-2}), \tag{6}$$

$$\tilde{h}^{\rm NR}_a(f) = \frac{1}{2}(\tilde{h}^{\rm CP}_{2,2} - \tilde{h}^{*\rm CP}_{2,-2}). \tag{7}$$

The symmetric and antisymmetric strains are complex quantities that can be written as

$$\tilde{h}^{\rm NR}_s(f) = A^{\rm NR}_s(f) e^{i\phi^{\rm NR}_s(f)}, \tag{8}$$

$$\tilde{h}^{\rm NR}_a(f) = A^{\rm NR}_a(f) e^{i\phi^{\rm NR}_a(f)} \tag{9}$$

and we can easily calculate their amplitude, $A^{\rm NR}$, and phase, $\phi^{\rm NR}$, as their absolute value and argument, respectively. We denote the ratio between the anti-symmetric and symmetric amplitudes as $\kappa_{\rm NR}(f) = A^{\rm NR}_a(f)/A^{\rm NR}_s(f)$.

IV. MODEL OF THE AMPLITUDE RATIO

We model the amplitude of the antisymmetric contribution $A_a(f)$ as a ratio of the symmetric contribution $A_s(f)$, i.e., $A_a(f) = \kappa(f) A_s(f)$.

Our first step in constructing the ratio model is to compute the ratio in the framework of PN theory as a PN expansion in terms of v/c, where v is the relative velocity of the two black holes and c is the speed of light, and we choose geometric units where $c = 1$. We again restrict our analysis to single-spin binaries.

To compute the PN ratio, we follow a procedure similar to the illustrative calculation in Sec. II. We obtain from Ref. [47] the complex 1.5PN expressions of the $(\ell=2,|m|=2)$ multipoles, $h^{PN}_{2\pm2}$, for spinning, precessing binaries with generic inclination angle ι moving on nearly circular orbits. The strains of the $\ell=|m|=2$ multipoles can then be transformed to a coprecessing frame that follows the instantaneous orbital plane. To achieve this, we choose a simple coprecessing frame where we set to zero the inclination angle of the orbital angular momentum relative to the total angular momentum, $\iota = 0$, and also set the precession angle, $\alpha = 0$. We then use an approximate reduction to a single-spin system [48],

$$\chi_{s/a,x} = -\chi \sin(\theta_{LS} - \iota)\cos(\alpha)/2, \tag{10}$$

$$\chi_{s/a,y} = -\chi \sin(\theta_{LS} - \iota)\sin(\alpha)/2, \tag{11}$$

$$\chi_{s/a,z} = \chi \cos(\theta_{LS} - \iota)/2, \tag{12}$$

where $\chi_s = (\chi_1 + \chi_2)/2$, $\chi_a = (\chi_1 - \chi_2)/2$ are the symmetric and antisymmetric spins defined in Ref. [47] and θ_{LS} is the inclination of the spin from the orbital angular momentum vector.

We then find that the symmetric and antisymmetric amplitudes are

$$A^{PN}_s(f) = -\frac{4M}{21D_L}\sqrt{\frac{\pi}{5}} v^2 \eta (42 + 84\pi v^3 + v^2(-107 + 55\eta) - 28 v^3 (1 + \delta - \eta)\chi \cos\theta_{LS}), \tag{13}$$

$$A^{PN}_a(f) = -\frac{2M}{D_L}\sqrt{\frac{\pi}{5}} v^4 (1+\delta)\eta\chi \sin\theta_{LS}. \tag{14}$$

The ratio of the two amplitudes is then given by

$$\kappa_{\rm PN}(f) = \frac{21 v^2 (1+\delta)\chi \sin\theta_{LS}}{2(42 + 84\pi v^3 + v^2(-107 + 55\eta) - 28 v^3 (1 + \delta - \eta)\chi \cos\theta_{LS})}, \tag{15}$$

where $\eta = m_1 m_2/M^2$ is the symmetric mass ratio and $\delta = (m_1 - m_2)/M > 0$ is a fractional mass difference. The expression of the PN ratio of the antisymmetric amplitude over the symmetric amplitude depends on the symmetric mass ratio, η, the spin magnitude, χ, and the angle θ_{LS} of the system. Consequently, Eq. (15) can be used to compute the PN ratio of any configuration as a function of frequency since $v = (\pi f M)^{1/3}$.

We cannot expect the PN estimate of the amplitude ratio, Eq. (15), to be accurate through merger and ringdown. To capture this behavior we investigated the addition of unknown higher-order terms and fit their coefficients to the NR data. The simplest approach is to add only one additional term, for example,

$$\kappa(f) = \kappa_{\rm PN}(f)(1 + b v^n), \tag{16}$$

where b is fit to the NR data. To do this it was necessary to choose an appropriate frequency range over which to perform the fit. The NR data are noisy in the early inspiral and in the post-ringdown frequencies, so we first identified a consistent definition of a frequency range that could be used for all 80 NR simulations, based on the ringdown frequency, f_{RD} of each NR configuration. The frequency range that we used in the final fits was given by $Mf_{\rm min} = (Mf_{RD} - 0.01)/5$ and $Mf_{\rm max} = Mf_{RD} - 0.002$.

We investigated fits to the amplitude ratio of the form Eq. (16) with $n = 3, 5, 7$. Figure 5 shows the results for one configuration, and illustrates that $n = 5$ provides the most accurate fit. In fact, we find that $n = 5$ consistently provides the most accurate fit across all 80 NR simulations.

It is also clear from Fig. 5 that our fit is not accurate beyond the ringdown frequency. Beyond this point the amplitude ratio appears to plateau. This is consistent with our expectations from perturbation theory, as discussed in Sec. II B, which predicts that the amplitude ratio will be constant throughout ringdown. To include this feature in our model, we fix $\kappa(f)$ to the value $\kappa(f_{RD})$ at frequencies $f > f_{RD}$. To avoid a sharp transition we use a moving average algorithm such that

$$\kappa_n(f) = \frac{1}{(2k+1)} \sum_{i=n-k+1}^{n+k+1} \kappa(f_i), \qquad n \in [k, N-k]. \tag{17}$$

We use a symmetric window of an equal number of points ($k = 40$) on either side of the frequency f to calculate the moving average. Here N is the length of the frequency series and the algorithm updates $\kappa(f)$ for $40 \leq n \leq N - 40$.

We fit the coefficient b in Eq. (16) (with $n = 5$) to each of the 80 single-spin NR waveforms from the NR catalog in Ref. [38]. Figure 6 shows the resulting fit for the amplitude ratio for the $(q = 1, \chi = 0.4, \theta_{LS} = 60°)$ configuration. We see that the final fit, including the leveling off of the amplitude ratio through ringdown, agrees well with the NR data. The lower panel of the figure shows the resulting estimate for the antisymmetric amplitude. We see that this

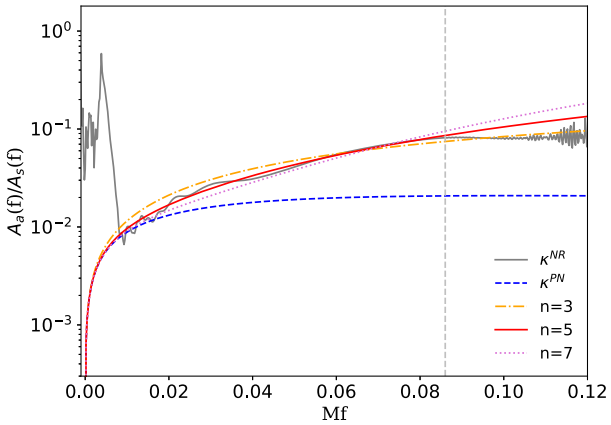

FIG. 5. Amplitude ratio for the $(q = 1, \chi = 0.4, \theta_{LS} = 60^o)$ configuration, for the NR data, the PN ratio $\kappa_{\rm PN}$, and fits to higher-order corrections as in Eq. (16), with $n = 3$, 5, 7. The vertical dashed line indicates the ringdown frequency.

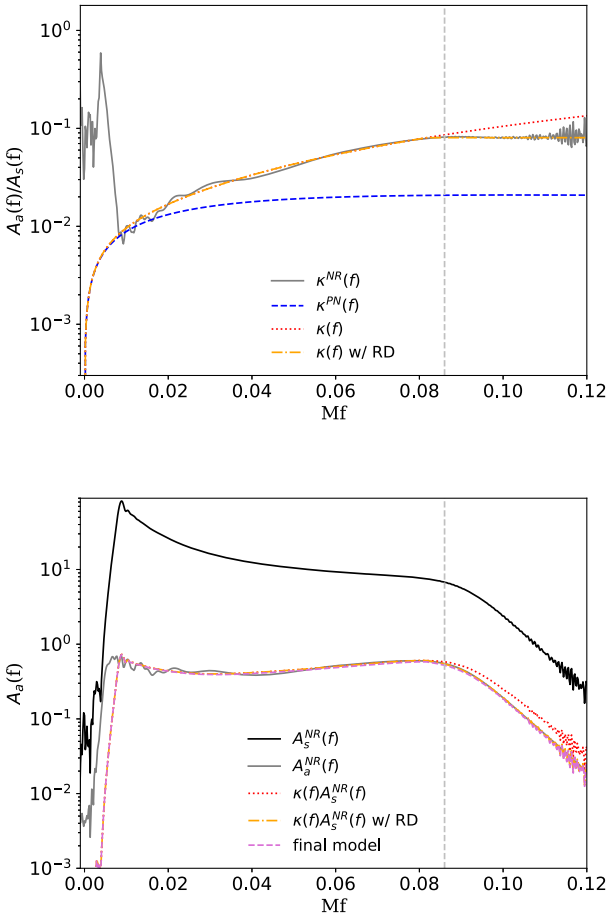

FIG. 6. The amplitude ratio (top) and amplitude (bottom) for the $(q = 1, \chi = 0.4, \theta_{LS} = 60°)$ configuration. The vertical line indicates the ringdown frequency for the $(\ell = 2, |m| = 2)$ multipoles.

agrees well with the NR data up to the point where the NR amplitude becomes dominated by noise.

The fit cannot reproduce the NR amplitude ratio in all cases. In many cases the NR amplitude ratio oscillates during the inspiral. Figure 7 shows an extreme example of this feature, from the $(q = 1, \chi = 0.8, \theta_{LS} = 30°)$ configuration. It is not clear what causes these oscillations. Oscillations in the coprecessing-frame amplitude ratio during the inspiral can be due to the choice of coprecessing frame, as we will discuss later. However, if that were the cause of the oscillations in the NR data, we would expect there to be some correlation with the degree of precession in the configuration. Instead we do not find any relationship between the amplitude of the oscillations, which in some cases are negligible (as in Fig. 6), and in others (like Fig. 7) lead to significant variations in the amplitude ratio. We do find, though, that our model passes through a reasonable estimate of the mean of the oscillations. The largest impact is on the constant value of the amplitude that the model settles on for the ringdown regime; in the example in Fig. 7 the model's estimate of the antisymmetric amplitude during the ringdown is roughly 20% below the NR value.

Finally, in some cases we also found that the amplitude ratio in the NR data did not level off during the ringdown. Figure 8 is an example of this. We have not been able to determine the reason for this. As noted previously, we expect that since the $(2, 2)$ and $(2, -2)$ multipoles decay at the same rate, that the ratio between their amplitudes would remain constant during the ringdown. It is possible that this effect is obscured by numerical noise. Regardless of the cause, and in the absence of any compelling explanation for alternative behavior, we have chosen to impose the behavior that we expect from perturbation theory.

The coefficient b is shown as a function of symmetric mass ratio and misalignment angle in Fig. 9; the values for all four spin magnitudes are shown together. This plot illustrates the general trend of b across the parameter space. We find that there is no general trend with respect to the spin magnitude, and this is illustrated more clearly in Fig. 10, which shows b as a function of symmetric mass

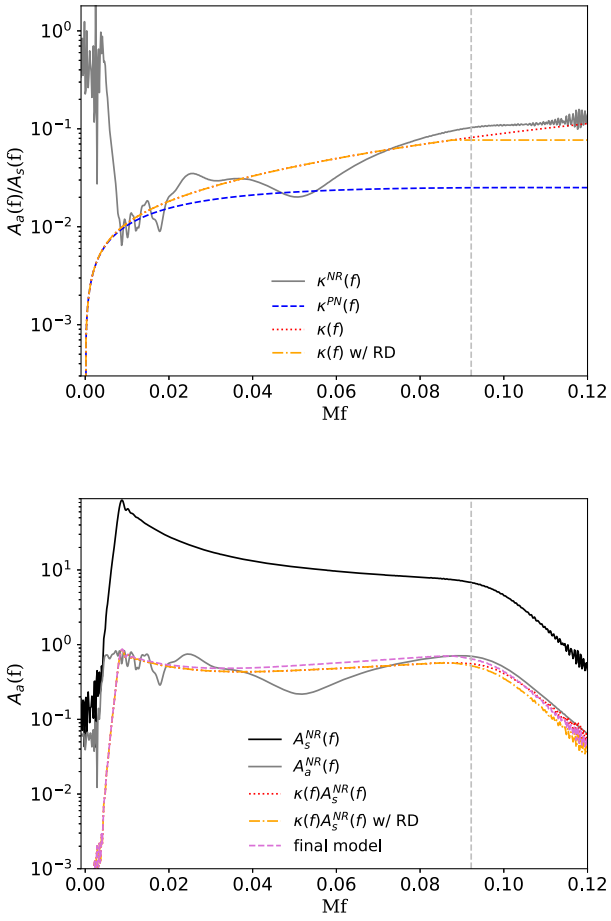

FIG. 7. The amplitude ratio (top) and amplitude (bottom) for the $(q = 1, \chi = 0.8, \theta_{LS} = 30°)$ configuration. The vertical line indicates the ringdown frequency for the $(\ell = 2, |m| = 2)$ multipoles.

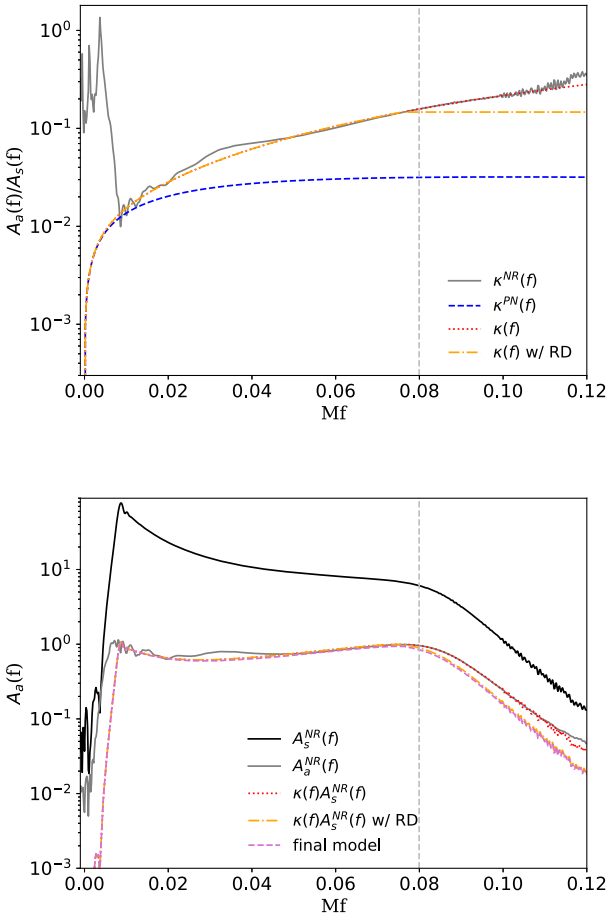

FIG. 8. The amplitude ratio (top) and amplitude (bottom) for the $(q = 2, \chi = 0.4, \theta_{LS} = 90°)$ configuration. The vertical line indicates the ringdown frequency for the $(\ell = 2, |m| = 2)$ multipoles.

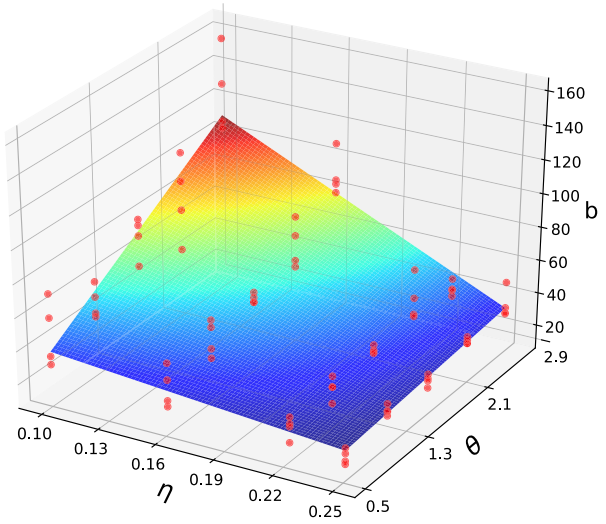

FIG. 9. Surface $b(\eta, \theta_{LS}) = b_0 + b_1\eta + b_2\theta_{LS} + b_3\eta\theta_{LS}$ fit of the model's coefficient, b, to the two-dimensional parameter space η, θ_{LS}. The red points denote the 80 computed b coefficients of the multipole asymmetry amplitude model.

ratio, for each spin magnitude, for the subset of cases with $\theta_{\rm LS} = 90°$. The PN amplitude ratio already includes a linear dependence on the spin magnitude, and given the uncertainty in our fits, we do not attempt to identify a higher-order spin dependence. We motivate this point further in Sec. VI (Fig. 14). We then include all simulations into a two-dimensional parameter-space fit of the form,

$$b(\eta, \theta_{\rm LS}) = b_0 + b_1\eta + b_2\theta_{\rm LS} + b_3\eta\theta_{LS}, \qquad (18)$$

where we find $b_0 = 18.0387$, $b_1 = 15.4509$, $b_2 = 55.1140$, and $b_3 = -203.6290$. From Eq. (18), we notice that b does not go to zero when θ_{LS} is 0° or 180°. However, the

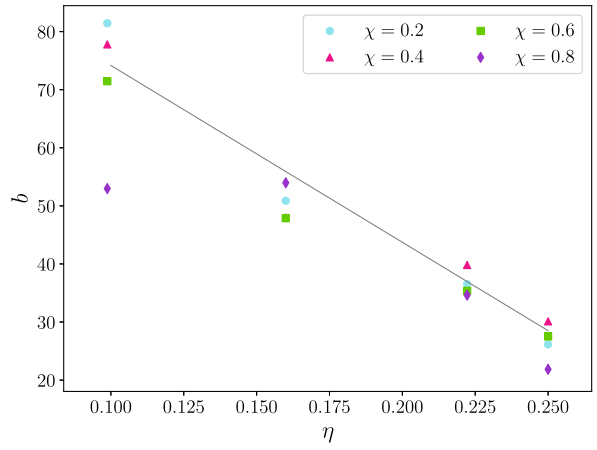

FIG. 10. The b coefficient as a function of the symmetric mass ratio, η, for a selected angle $\theta_{LS} = 90^o$ and all the available spin values, $\chi = [0.2, 0.4, 0.6, 0.8]$. The gray line shows the surface fit, $b(\eta, 90°)$ from Eq. (18).

presence of the $\sin\theta_{LS}$ term at the numerator of the ansatz of the ratio model in Eq. (15) ensures that the multipole asymmetry goes to zero at these points. The amplitude as predicted by this fit is shown on each of our figures and labeled as "final model."

Two caveats to this approach are worth noting. One is the choice of coprecessing frame. Previous work has shown that the symmetric (2, 2) contribution takes a simple form in the QA coprecessing frame; indeed, the amplitude evolution can be approximated by the (monotonic) amplitude of an equivalent aligned-spin configuration. This is not necessarily the case for the antisymmetric contribution, and this is one possible cause of the oscillations that we see (although, as noted previously, it does not show a clear correlation with the strength of precession). Conversely, we found that the amplitude evolution of the antisymmetric (2, 2) multipole was monotonic for PN waveforms if we choose $\iota = \alpha = 0$ in their construction (which is equivalent to choosing a coprecessing frame that tracks the Newtonian orbital angular momentum, i.e., the normal to the orbital plane), but if we consider the PN waveforms in the QA frame then the antisymmetric (2, 2) amplitude shows strong modulations. This illustrates that the antisymmetric component can depend strongly on the choice of coprecessing frame, and although we do not expect this to be a significant issue at the level of accuracy or approximation of the current model, it may require better understanding in future refinements of antisymmetric models.

The second point is that our model is constructed based on the phenomenology of single-spin binaries. If the model is to be used for generic binaries, one must choose a method to treat two-spin configurations. One option, which is employed in the `PhenomX` implementation [48,49], is as follows.

We can describe the spin of an equivalent single-spin system using Eqs. (16) and (17) in Ref. [48], but diverge slightly in the definition of the in-plane spin as follows:

$$\chi^{\perp} = \begin{cases} \chi_{\rm as}\cos^2(\theta_q) + \chi_{\rm p}\sin^2(\theta_q), & 1 \le q \le 1.5 \\ \chi_{\rm p}, & q > 1.5 \end{cases}, \qquad (19)$$

where $\chi_{\rm p}$ is the effective precession spin as defined in Ref. [56]. The antisymmetric amplitude for an equal-mass binary with both spins equal in magnitude, entirely in-plane and pointing in the same direction, must drop to zero. The symmetric in-plane spin combination of Eq. (15) in Ref. [48] cannot account for this effect in superkick configuration. Therefore, we can instead use an antisymmetric in-plane spin combination,

$$\chi_{\rm as} = \frac{|\mathbf{S}_1^{\perp} - \mathbf{S}_2^{\perp}|}{m_1^2}, \qquad (20)$$

to appropriately map two-spin to single-spin systems for generating the antisymmetric waveform.

V. PHASE MODEL

GW phases for chirp signals in the frequency domain are typically quite featureless and therefore not conducive to modeling. Following a suite of models for the symmetric phase [11,12,17], we focus first on the antisymmetric phase derivative. Figure 11 demonstrates that the antisymmetric phase derivative (i.e., frequency) behavior in the time domain as discussed in Sec. II B is preserved in the frequency domain as well. Remarkably, we find that it is possible to construct a map of the symmetric phase derivative to the antisymmetric phase derivative that is independent of the binary's parameters. Therefore, we do not need to produce any parametric fits for the map over the intrinsic parameter space of BH binaries, which makes this model extremely simple.

Our model of the antisymmetric phase derivative is defined by the piecewise function,

$$\phi'_a(f) = \begin{cases} \frac{1}{2}\phi'_s(f) + \alpha'(f) + A_0, & f \le f_T - \frac{f_w}{2} \\ \phi'_{\rm int}(f), & f_T - \frac{f_w}{2} < f \le f_T + \frac{f_w}{2}, \\ \phi'_s(f), & f_T + \frac{f_w}{2} \le f < 0.12 \end{cases} \tag{21}$$

where the phase derivative in the intermediate region is given by

$$\begin{aligned} \phi'_{\rm int}(f) = {} & \frac{1}{2}\left[1 - \frac{3}{2f_w}\left((f-f_T) - \frac{(f-f_T)^3}{3f_w^2}\right)\right] \\ & \times \left(\frac{\phi'_s}{2} + \alpha' + A_0\right) \\ & + \frac{1}{2}\left[1 + \frac{3}{2f_w}\left((f-f_T) - \frac{(f-f_T)^3}{3f_w^2}\right)\right](\phi'_s + B_0). \end{aligned} \tag{22}$$

As is evident from Fig. 11, the functional form of region I transitions to the functional form of region II in the intermediate region. To ensure smooth transition in the intermediate region an obvious choice would be a tanh windowing function. Noting that a tanh function can be computationally inefficient during model evaluation, we instead use the Taylor expansion of the tanh function up to second order with appropriate normalization to construct the phase derivative functional form of Eq. (22).

The phase derivative ansatz was calibrated to NR simulations by treating the transition frequency, f_T, the width of the transition window, f_w, and the phase coefficients (A_0 and B_0) as free parameters. The window parameters were not particularly sensitive to the tuning and the minor variations could be attributed to the noise in the antisymmetric phase derivatives; $f_T = 0.85 f_{RD}$ and $f_w = 0.005$ was found to be an optimal choice across the entire single-spin parameter space.

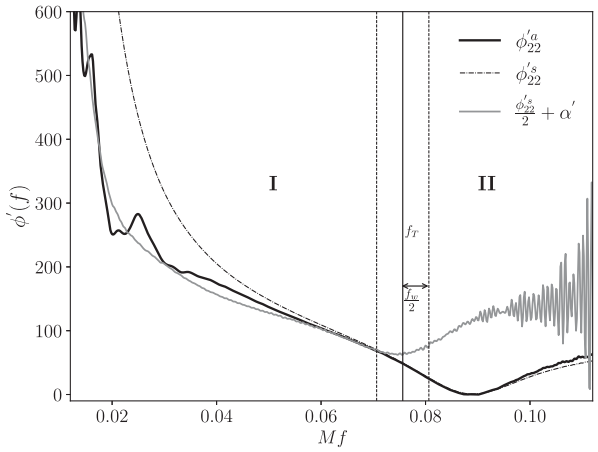

FIG. 11. The antisymmetric phase derivative (thick black line), the symmetric phase derivative (gray dashed line) and the combination of half of the symmetric phase derivative with the derivative of the precession angle α (thin gray line). The specific configuration shown here is for a single-spin binary with ($q = 1$, $\chi = 0.2$, $\theta_{LS} = 30°$).

Once the parameters of the window function were fixed, we investigated the impact of fixing the phase coefficients. A best fit to data for $B_0 = 0$ was found to be consistent across the parameter space; A_0 on the other hand showed some variation, but no specific trend. Furthermore, choosing the algebraic mean of A_0 for the set of 80 simulations did not significantly impact the quality of the fit. This shows (1) the fitting algorithm tries to find the best A_0 for continuity of the phase derivative at f_T, and (2) the variation in optimal A_0 across the parameter space is more likely due to noisy data and not a function of intrinsic parameters of the binary.

Applying a shift to the phase derivative is equivalent to an overall time shift of the waveform. We exploit this freedom by fixing the symmetric phase derivative minima to be 0 at f_{RD}. This imposes

$$A_0 = \frac{1}{2}\phi'_s(f_T) - \alpha'(f_T). \tag{23}$$

Figure 12 shows that A_0 obtained from the fitting algorithm and from NR data using Eq. (23) reasonably well for a majority of the cases (cf. y axis on Fig. 11). The antisymmetric model will be used with a phenomenological symmetric waveform model, so an A_0 derived from the symmetric waveform model makes the phase construction self-consistent and robust. Furthermore, Fig. 12 highlights that the gain in accuracy by making a model to capture the near-stochastic behavior of A_0 may be outweighed by errors introduced by overmodeling. As such, our model of the antisymmetric phase is NR informed but, noting that the data for the antisymmetric waveform is often close to numerical noise, we prioritized our understanding of the physics rather than model optimization.

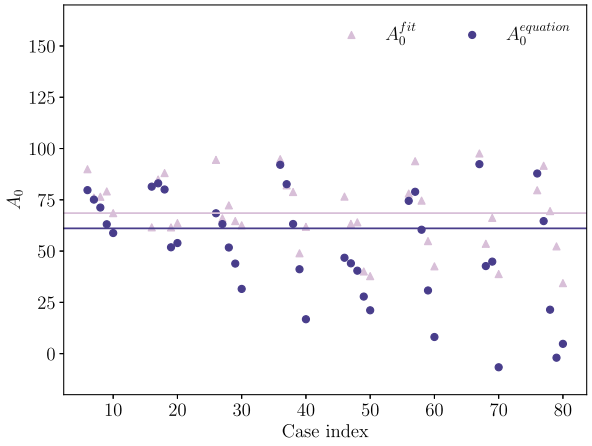

FIG. 12. Comparison of phase coefficient A_0, obtained from fitting the phase ansatz to NR data (light purple triangles) across the parameter space and from NR data using Eq. (23) (blue circles), for cases with $\chi = 0.4$ and 0.8. The algebraic mean of the set of coefficients are shown by horizontal lines in corresponding colors. The case index is as described in Sec. III.

The phase of the antisymmetric waveform is obtained by integrating the two pieces,

$$\phi_a(f) = \begin{cases} \frac{1}{2}\phi_s(f) + \alpha(f) + A_0 f + \phi_{A0}, & f \le f_T \\ \phi_s(f) + \phi_{B0}, & f_T \le f < 0.12 \end{cases}, \tag{24}$$

where the integration constant ϕ_{B0} is determined by continuity at f_T

$$\phi_{B0} = \alpha(f_T) - \phi_s(f_T) + A_0 f_T. \tag{25}$$

Finally, the phase of the asymmetry is modulated by the in-plane spin direction α; therefore, the initial phase, ϕ_{A0}, is the value of α at a reference frequency, i.e., $\phi_{A0} = \alpha(f_{\rm ref})$.

VI. MODEL ACCURACY

A standard measure of waveform accuracy used extensively in the literature is the match of the waveform model with NR waveforms, defined as

$$M(h_{\rm NR}, h_M) = 4{\rm Re}\int_0^\infty \frac{{\rm h_{NR}}(f){\rm h_M^*}(f)}{{\rm S_n}(f)}{\rm d}f, \tag{26}$$

where $h(f) = h_+(f) - ih_\times(f)$ is a complex frequency sequence constructed from the two polarizations of the waveform, and an optimization over time and phase is implied. As such, calculating matches of just the antisymmetric waveform is not physically meaningful. Furthermore, a true measure of performance of precessing waveforms in data analysis can only be obtained by calculating matches of the full waveform in the inertial frame, making considerations for precession as well as extrinsic parameters. Therefore, matches of just the antisymmetric waveform in the coprecessing frame provide some indication of the accuracy of one ingredient in the full waveform, but do not indicate the overall accuracy of the corresponding precessing waveform.

However, an inner product like that in Eq. (26) is a useful measure of agreement between two complex frequency

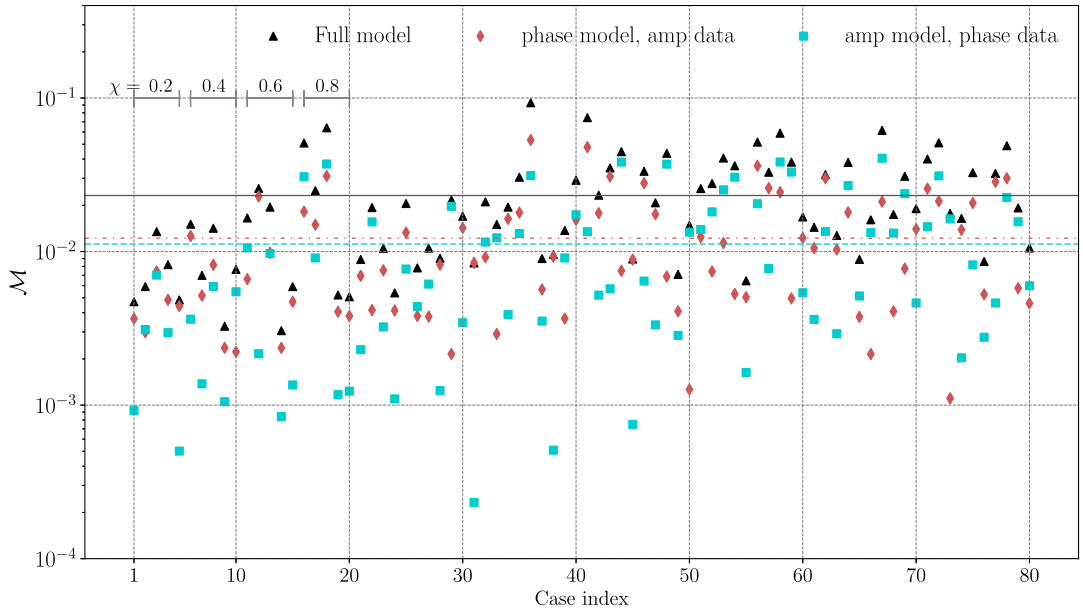

FIG. 13. Mismatches of the antisymmetric waveform model in the coprecessing frame with NR data. The black triangles show the mismatches for the combined amplitude and phase model while the cyan squares (brown diamonds) show the mismatches for just the amplitude (phase) model with the phase (amplitude) constructed from NR data. The dashed cyan line and the dashed-dotted brown line show the average mismatch for the amplitude and phase model, respectively; on average they are of comparable accuracy. The black solid line shows the average mismatch for the overall model. The x axis denotes the case index of the NR simulation as usual, i.e., five different $\theta_{\rm LS}$ for each spin magnitude shown in the figure and mass ratio $q = 1$, 2, 4, and 8.

series. Since a match-like calculation for the antisymmetric contribution in the coprecessing frame cannot be interpreted in terms of either signal detection efficiency or parameter measurement accuracy, there is no reason to include the detector sensitivity, and so we will use a simpler inner product of the form,

$$\langle h_{\rm NR}|h_M\rangle = {\rm Re}\int_{f_1}^{f_2} {\rm h}_{\rm NR}(f){\rm h}^*_{\rm M}(f){\rm d}f, \tag{27}$$

where f_1 is the starting frequency of the NR waveform in geometric units, $Mf_1 = 0.02$, and $Mf_2 = 0.15$, after which point the amplitude of the NR waveform is below the noise floor of the data. We consider normalized waveforms, $\hat{h} = h/\sqrt{\langle h|h\rangle}$, so that the maximum value of the inner product is one. We used the standard implementation of this inner product in PYCBC [57], a Python software package for GW data analysis, for our match computations. We then consider the "mismatch" between the two waveforms,

$$\mathcal{M} = 1 - \frac{\langle h_{\rm NR}|h_M\rangle}{\sqrt{\langle h_{\rm NR}|h_{\rm NR}\rangle\langle h_M|h_M\rangle}}. \tag{28}$$

In Fig. 13 we show the mismatches of the antisymmetric waveform constructed from our model with the 80 NR waveforms that were used to calibrate the model. To determine the accuracy of the individual components, we also computed matches of the amplitude (phase) model complemented by phase (amplitude) constructed from NR data, with the full antisymmetric waveform constructed from NR data. The overall accuracy of both the models are comparable. We note that although the model was verified using the same waveforms as used for modeling, since the NR tuning was relatively simple—i.e., a single coefficient in Eq. (16) fit to the four-parameter ansatz Eq. (18) across a two-dimensional parameter space—using a much smaller subset of waveforms would have produced a model of similar accuracy, and the simplicity of this model and the single-spin parameter space obviates any concerns about overfitting or unexplored corners of parameter space.

To investigate the quality of the surface fit in Eq. (18), we also computed mismatches for the amplitude model using fit coefficients b of Eq. (16). As is evident from Fig. 14, for most cases the performance is unchanged and for the handful of cases where the mismatch changes, the difference is not very significant. This further illustrates that capturing the nonlinear dependence on spin magnitude is unlikely to make significant improvement to the amplitude model. In addition to the argument made for using Eq. (23) to calculate A_0 from the symmetric waveform and precession angle, α, we calculated mismatches for the different choices of A_0 in the phase model—i.e., $A_0^{\rm fit}$ and $A_0^{\rm equation}$ in Fig. 12—to confirm that there was no reduction in model accuracy.

Note that the antisymmetric waveform model is downstream from the symmetric waveform model as well as the precession angle models. Therefore, enhancement in performance of the overall model due to the addition of an asymmetry model must always be discussed in the context of the underlying symmetric, precessing waveform model. This is beyond the scope of present work and will be

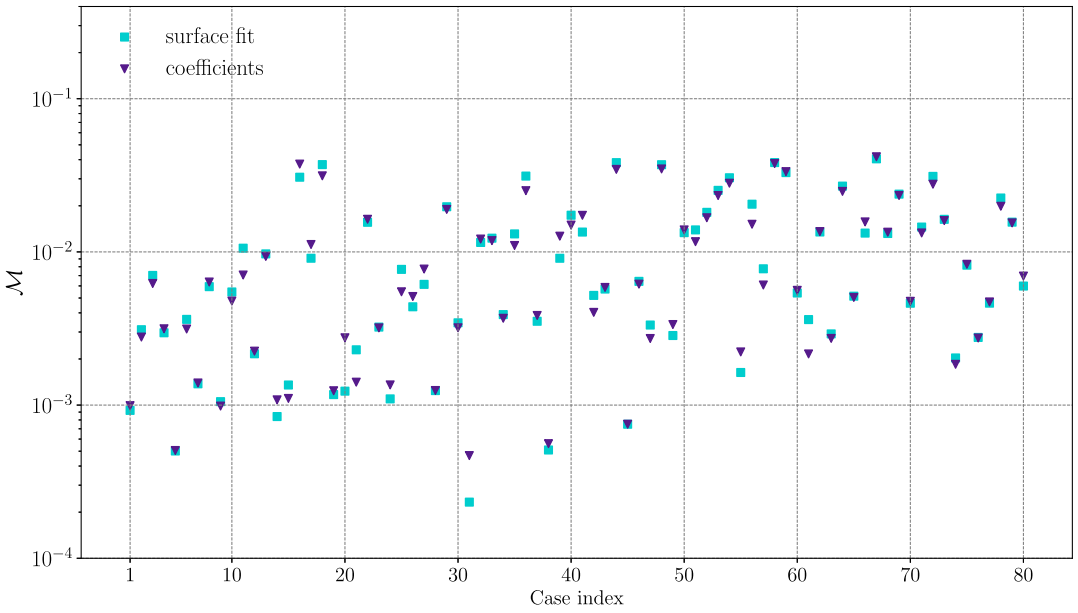

FIG. 14. Mismatches (same as Fig. 13) showing comparison of the amplitude model constructed using the spin magnitude-independent surface fit of Eq. (16) (cyan squares) with the amplitude model constructed from the true fit coefficients (violet inverted triangles). The phase of the antisymmetric waveform is constructed from NR data for both cases.

discussed in the context of the current generation frequency-domain precessing-binary PhenomXPNR model [49].

VII. CONCLUSION

We have presented a method to model the antisymmetric contribution to the $(\ell = 2, |m| = 2)$ multipoles in the coprecessing frame. This is a general approach that can be applied to any frequency-domain model that provides the symmetric contribution to the (2, 2) amplitude, phase, and precession angle, α. We expect that the main insights of this model can be used to easily generalize the procedure to the time domain and be useful in including multipole asymmetry in current generation time-domain models [45,46]. We summarize the key insights here.

For the amplitude, we observe that the antisymmetric amplitude can be easily modeled as a rescaling of the symmetric amplitude. As shown in Fig. 4, both amplitudes have the same basic structure, in particular the same ringdown frequency and decay rate. In the inspiral our model of the amplitude ratio is based on a PN expression for single-spin systems, and in the late inspiral and merger a higher-order correction to the PN expression is calibrated to 80 NR simulations of single-spin binaries [38]. In the ringdown we make use of the prediction from perturbation theory that the ratio of the symmetric and antisymmetric amplitudes will be constant. The amplitude model ratio is presented in Eqs. (15) and (16) and the fit to the higher-order contribution given in Eq. (18).

For the phase, we use the facts that in the inspiral the frequency of the antisymmetric contribution equals the orbital frequency plus the spin precession frequency, and that during the ringdown the symmetric and antisymmetric frequencies are the same. We are able to construct a mapping from the symmetric phase and precession angle, ϕ_s and α, to the antisymmetric phase, ϕ_a, motivated by the 80 single-spin simulations, but without the need of any explicit tuning. The model of the phase is given in Eqs. (23)–(25). An additional crucial observation is that a rotation of the initial in-plane spin direction of $\Delta\alpha$ introduces a corresponding shift of $\Delta\alpha$ into the antisymmetric phase. It is this observation that allows us to model the dependence on in-plane-spin direction, even though we do not have a set of NR simulations that span this subspace.

The procedure presented here is not in itself a signal model. As already noted, one must also provide the symmetric amplitude, phase and precession angle. In addition, having constructed a model for the antisymmetric contribution to the (2, 2) multipoles in the coprecessing frame, one must then "twist them up" to produce the multipoles in the inertial frame. This has been done for the recent extension of the multimode frequency-domain precessing-binary IMRPhenomXPNR model [49].

This is the first phenomenological full inspiral-merger-ringdown model of the antisymmetric multipole contributions, and there are many directions for improvement and issues to be resolved. The first limitation of the model is that it is based only on single-spin binaries. We expect that generic two-spin systems can in most cases be modeled to a good approximation by single-spin systems, but given that the antisymmetric contribution is itself a weak effect, it is unclear how well this approximation can be used. It would be useful to study the applicability of the single-spin approximation for the antisymmetric contribution, and, indeed, to extend the model to two-spin systems. The antisymmetric model is also limited to the $(\ell = 2, |m| = 2)$ multipoles. We argue in Fig. 1 that the (2, 2) contribution will be sufficient for most applications, since the antisymmetric amplitude is far weaker than the symmetric, but for high SNR systems, higher-order antisymmetric multipoles will ultimately be required.

When decomposing the signal into a coprecessing frame and corresponding time- or frequency-dependent angles, one will find (depending on the coprecessing frame chosen) oscillations in the amplitude and/or phase of the antisymmetric contribution; recall that the coprecessing frame maps exactly to a nonprecessing aligned-spin waveform only for the leading-order quadrupole terms [44,48,49]. In this work we have removed oscillations in the inspiral amplitude by simply setting the inclination angle ι and precession angle α to zero in the PN expressions we have used for the signal multipoles [47]; oscillations remain in the coprecessing-frame signals for the NR waveforms, but our model consists of only a monotonic fit through these oscillations. A better understanding of these oscillations, or at least a model that captures them, is a necessary next step in modeling the multipole asymmetries.

We have assumed that the only affect of the initial in-plane spin direction is to introduce an overall offset in the antisymmetric phase. This approximation will not be exact during the merger ringdown. In particular, in the ringdown we have made the approximation that the amplitude ratio will be independent of the initial in-plane spin direction. However, the amplitude ratio will be determined by the relative phase of the symmetric and antisymmetric contributions when ringdown begins, and we have not attempted to model this effect.

These limitations aside, we find that our method to construct the antisymmetric contribution has an average mismatch error better than 0.03. Given that the antisymmetric contribution is in general less than 10% of the total SNR, we expect that its contribution to the total mismatch uncertainty of a model will be less than 3×10^{-3}, which is below the average mismatch error of current Phenom and SEOBNR precessing-binary models [46,49]. With the addition of this first antisymmetric model, we expect that current models will be able to make more precise measurements of black-hole spins and gravitational recoil. The accuracy of these measurements will depend significantly on the underlying symmetric model, as well as where a signal lies in the binary parameter space, and we leave such accuracy studies with individual models to future work.

ACKNOWLEDGMENTS

We thank Jonathan Thompson, Eleanor Hamilton, and Lionel London for many thought-provoking discussions on precession. We are indebted to Lionel London for sharing his numerical relativity data utility package with us. We thank Frank Ohme and Jannik Mielke for insightful discussions on multipole asymmetry, and Chinmay Kalaghatgi for discussions on in-plane spin rotation in superkick configurations. We are also grateful to Sebastian Khan, Frank Ohme, and Lucy Thomas for useful comments on the draft. S. G. thanks Sebastian Khan for stimulating discussions on frequency-domain waveform modeling, Duncan Macleod for excellent inputs on computing practices, and Edward Fauchon-Jones for support in using supercomputing facilities. The authors were supported in part by Science and Technology Facilities Council (STFC) Grant No. ST/V00154X/1 and European Research Council (ERC) Consolidator Grant No. 647839. S. G. acknowledges support from the Max Planck Society's Independent Research Group program. P. K. was also supported by the GW consolidated grant: STFC Grant No. ST/V005677/1. Simulations used in this work were performed on the DiRAC@Durham facility, managed by the Institute for Computational Cosmology on behalf of the STFC DiRAC HPC Facility ([58]). The equipment was funded by BEIS capital funding via STFC capital Grants No. ST/P002293/1 and No. ST/R002371/1, Durham University and STFC operations Grant No. ST/R000832/1. In addition, several of the simulations used in this work were performed as part of an allocation graciously provided by Oracle to explore the use of our code on the Oracle Cloud Infrastructure. This research also used the supercomputing facilities at Cardiff University operated by Advanced Research Computing at Cardiff (ARCCA) on behalf of the Cardiff Supercomputing Facility and the HPC Wales and Supercomputing Wales (SCW) projects. We acknowledge the support of the latter, which is partly funded by the European Regional Development Fund (ERDF) via the Welsh Government. In part the computational resources at Cardiff University were also supported by STFC Grant No. ST/I006285/1. Various plots and analyses in this paper were made using Python software packages LALSuite [59], PyCBC [57], GWSURROGATE [60], Matplotlib [61], NumPy [62], and LMFIT and SciPy [63].

[1] B. P. Abbott *et al.* (LIGO Scientific and Virgo Collaborations), Phys. Rev. X **9**, 031040 (2019).
[2] R. Abbott *et al.* (LIGO Scientific and Virgo Collaborations), Phys. Rev. X **11**, 021053 (2021).
[3] R. Abbott *et al.* (LIGO Scientific, Virgo, and KAGRA Collaborations), Phys. Rev. X **13**, 041039 (2023).
[4] B. P. Abbott *et al.* (LIGO Scientific and Virgo Collaborations), Phys. Rev. Lett. **116**, 061102 (2016).
[5] B. P. Abbott *et al.* (LIGO Scientific and Virgo Collaborations), Astrophys. J. Lett. **818**, L22 (2016).
[6] B. P. Abbott *et al.* (LIGO Scientific and Virgo Collaborations), Astrophys. J. Lett. **882**, L24 (2019).
[7] R. Abbott *et al.* (LIGO Scientific and Virgo Collaborations), Astrophys. J. Lett. **913**, L7 (2021).
[8] R. Abbott *et al.* (KAGRA, Virgo, and LIGO Scientific Collaborations), Phys. Rev. X **13**, 011048 (2023).
[9] M. Pürrer, M. Hannam, and F. Ohme, Phys. Rev. D **93**, 084042 (2016).
[10] S. Khan, F. Ohme, K. Chatziioannou, and M. Hannam, Phys. Rev. D **101**, 024056 (2020).
[11] S. Husa, S. Khan, M. Hannam, M. Pürrer, F. Ohme, X. Jiménez Forteza, and A. Bohé, Phys. Rev. D **93**, 044006 (2016).
[12] S. Khan, S. Husa, M. Hannam, F. Ohme, M. Pürrer, X. Jiménez Forteza, and A. Bohé, Phys. Rev. D **93**, 044007 (2016).
[13] M. Hannam, P. Schmidt, A. Bohé, L. Haegel, S. Husa, F. Ohme, G. Pratten, and M. Pürrer, Phys. Rev. Lett. **113**, 151101 (2014).
[14] L. London, S. Khan, E. Fauchon-Jones, C. García, M. Hannam, S. Husa, X. Jiménez-Forteza, C. Kalaghatgi, F. Ohme, and F. Pannarale, Phys. Rev. Lett. **120**, 161102 (2018).
[15] S. Khan, K. Chatziioannou, M. Hannam, and F. Ohme, Phys. Rev. D **100**, 024059 (2019).
[16] S. Khan, F. Ohme, K. Chatziioannou, and M. Hannam, Phys. Rev. D **101**, 024056 (2020).
[17] G. Pratten, S. Husa, C. Garcia-Quiros, M. Colleoni, A. Ramos-Buades, H. Estelles, and R. Jaume, Phys. Rev. D **102**, 064001 (2020).
[18] C. García-Quirós, M. Colleoni, S. Husa, H. Estellés, G. Pratten, A. Ramos-Buades, M. Mateu-Lucena, and R. Jaume, Phys. Rev. D **102**, 064002 (2020).
[19] G. Pratten *et al.*, Phys. Rev. D **103**, 104056 (2021).
[20] J. E. Thompson, E. Fauchon-Jones, S. Khan, E. Nitoglia, F. Pannarale, T. Dietrich, and M. Hannam, Phys. Rev. D **101**, 124059 (2020).
[21] H. Estellés, A. Ramos-Buades, S. Husa, C. García-Quirós, M. Colleoni, L. Haegel, and R. Jaume, Phys. Rev. D **103**, 124060 (2021).
[22] H. Estellés, S. Husa, M. Colleoni, D. Keitel, M. Mateu-Lucena, C. García-Quirós, A. Ramos-Buades, and A. Borchers, Phys. Rev. D **105**, 084039 (2022).
[23] A. Taracchini, Y. Pan, A. Buonanno, E. Barausse, M. Boyle, T. Chu, G. Lovelace, H. P. Pfeiffer, and M. A. Scheel, Phys. Rev. D **86**, 024011 (2012).
[24] Y. Pan, A. Buonanno, A. Taracchini, L. E. Kidder, A. H. Mroué, H. P. Pfeiffer, M. A. Scheel, and B. Szilágyi, Phys. Rev. D **89**, 084006 (2014).

[25] A. Taracchini *et al.*, Phys. Rev. D **89**, 061502 (2014).
[26] A. Bohé *et al.*, Phys. Rev. D **95**, 044028 (2017).
[27] R. Cotesta, A. Buonanno, A. Bohé, A. Taracchini, I. Hinder, and S. Ossokine, Phys. Rev. D **98**, 084028 (2018).
[28] S. Ossokine *et al.*, Phys. Rev. D **102**, 044055 (2020).
[29] A. Matas *et al.*, Phys. Rev. D **102**, 043023 (2020).
[30] T. A. Apostolatos, C. Cutler, G. J. Sussman, and K. S. Thorne, Phys. Rev. D **49**, 6274 (1994).
[31] B. Bruegmann, J. A. Gonzalez, M. Hannam, S. Husa, and U. Sperhake, Phys. Rev. D **77**, 124047 (2008).
[32] M. Hannam *et al.*, Nature (London) **610**, 652 (2022).
[33] V. Varma, S. Biscoveanu, T. Islam, F. H. Shaik, C.-J. Haster, M. Isi, W. M. Farr, S. E. Field, and S. Vitale, Phys. Rev. Lett. **128**, 191102 (2022).
[34] C. Kalaghatgi and M. Hannam, Phys. Rev. D **103**, 024024 (2021).
[35] A. Ramos-Buades, P. Schmidt, G. Pratten, and S. Husa, Phys. Rev. D **101**, 103014 (2020).
[36] P. Kolitsidou, J. E. Thompson, and M. Hannam (to be published).
[37] V. Varma, S. E. Field, M. A. Scheel, J. Blackman, D. Gerosa, L. C. Stein, L. E. Kidder, and H. P. Pfeiffer, Phys. Rev. Res. **1**, 033015 (2019).
[38] E. Hamilton *et al.*, arXiv:2303.05419 [Phys. Rev. D (to be published)].
[39] L. E. Kidder, Phys. Rev. D **52**, 821 (1995).
[40] J. A. Gonzalez, M. D. Hannam, U. Sperhake, B. Bruegmann, and S. Husa, Phys. Rev. Lett. **98**, 231101 (2007).
[41] M. Campanelli, C. O. Lousto, Y. Zlochower, and D. Merritt, Phys. Rev. Lett. **98**, 231102 (2007).
[42] D. Keppel, D. A. Nichols, Y. Chen, and K. S. Thorne, Phys. Rev. D **80**, 124015 (2009).
[43] M. Boyle, L. E. Kidder, S. Ossokine, and H. P. Pfeiffer, arXiv:1409.4431.
[44] P. Schmidt, M. Hannam, and S. Husa, Phys. Rev. D **86**, 104063 (2012).
[45] H. Estellés, M. Colleoni, C. García-Quirós, S. Husa, D. Keitel, M. Mateu-Lucena, M. d. L. Planas, and A. Ramos-Buades, Phys. Rev. D **105**, 084040 (2022).
[46] A. Ramos-Buades, A. Buonanno, H. Estellés, M. Khalil, D. P. Mihaylov, S. Ossokine, L. Pompili, and M. Shiferaw, Phys. Rev. D **108**, 124037 (2023).
[47] K. G. Arun, A. Buonanno, G. Faye, and E. Ochsner, Phys. Rev. D **79**, 104023 (2009); **84**, 049901(E) (2011).
[48] E. Hamilton, L. London, J. E. Thompson, E. Fauchon-Jones, M. Hannam, C. Kalaghatgi, S. Khan, F. Pannarale, and A. Vano-Vinuales, Phys. Rev. D **104**, 124027 (2021).
[49] J. E. Thompson, E. Hamilton, L. London, S. Ghosh, P. Kolitsidou, C. Hoy, and M. Hannam, arXiv:2312.10025.
[50] B. Bruegmann, J. A. Gonzalez, M. Hannam, S. Husa, U. Sperhake, and W. Tichy, Phys. Rev. D **77**, 024027 (2008).
[51] S. Husa, J. A. Gonzalez, M. Hannam, B. Bruegmann, and U. Sperhake, Classical Quantum Gravity **25**, 105006 (2008).
[52] L. London, NRUTILS, https://github.com/llondon6/nrutils_dev (2015).
[53] P. Schmidt, M. Hannam, S. Husa, and P. Ajith, Phys. Rev. D **84**, 024046 (2011).
[54] R. O'Shaughnessy, B. Vaishnav, J. Healy, Z. Meeks, and D. Shoemaker, Phys. Rev. D **84**, 124002 (2011).
[55] M. Boyle, R. Owen, and H. P. Pfeiffer, Phys. Rev. D **84**, 124011 (2011).
[56] P. Schmidt, F. Ohme, and M. Hannam, Phys. Rev. D **91**, 024043 (2015).
[57] A. Nitz *et al.*, GWASTRO/PyCBC: PyCBC release 1.18.1, (2021).
[58] www.dirac.ac.uk.
[59] LIGO Scientific Collaboration, LIGO Algorithm Library—LALSuite, free software (GPL), 10.7935/GT1W-FZ16 (2018).
[60] S. E. Field, C. R. Galley, J. S. Hesthaven, J. Kaye, and M. Tiglio, Phys. Rev. X **4**, 031006 (2014).
[61] J. D. Hunter, Comput. Sci. Eng. **9**, 90 (2007).
[62] C. R. Harris *et al.*, Nature (London) **585**, 357 (2020).
[63] P. Virtanen *et al.* (SciPy 1.0 Contributors), Nat. Methods **17**, 261 (2020).